Available online at www.sciencedirect.com

jmr&t Journal of Materials Research and Technology

journal homepage: www.elsevier.com/locate/jmrt

Original Article

Microstructure and corrosion resistance of highly <111> oriented electrodeposited CoNiFe medium-entropy alloy films

Wenyi Huo [a,b,*], Shiqi Wang [c], Feng Fang [c,**], Shuyong Tan [d], Łukasz Kurpaska [b], Zonghan Xie [e], Hyoung Seop Kim [f], Jianqing Jiang [a,c]

[a] College of Mechanical and Electrical Engineering, Nanjing Forestry University, Nanjing, 210037, China
[b] NOMATEN Centre of Excellence, National Centre for Nuclear Research, Otwock, 05-400, Poland
[c] School of Materials Science and Engineering, Southeast University, Nanjing, 211189, China
[d] Jiangsu Key Laboratory of Advanced Structural Materials and Application Technology, Nanjing Institute of Technology, Nanjing, 211167, China
[e] School of Mechanical Engineering, University of Adelaide, Adelaide, SA 5005, Australia
[f] Department of Materials Science and Engineering, Pohang University of Science & Technology (POSTECH), Pohang, 37673, South Korea

ARTICLE INFO

Article history:
Received 18 March 2022
Accepted 22 July 2022
Available online 8 August 2022

Keywords:
Medium-entropy alloy
Compositionally complex alloy
CoNiFe film
Corrosion resistance
Electrodeposition

ABSTRACT

The medium-entropy alloy is a newly intriguing material showing superb properties. A simple, one-step method was developed to electrodeposit CoNiFe medium-entropy alloy films from a sulfate and citrate bath. The microstructure and corrosion resistance were investigated in CoNiFe films with varying deposition current densities. It shows the face-centered cubic structure with a <111> preferential orientation. HRTEM-EDS observations further show information on the nanostructure and element distribution. The films exhibit a strong corrosion resistance in 3.5 wt.% NaCl solution. The films electrodeposited with a current density of 44.4 A/dm^2 shows a low self-corrosion current density of 4.72×10^{-6} A•cm^{-2} in 3.5 wt.% NaCl solution. The corrosion mechanism was proposed in combination with electrochemical impedance spectroscopy results. The outstanding properties were attributed to the near-equimolar ternary components. The results lay a solid foundation for developing of highly oriented medium-entropy alloy films with strong corrosion resistance.

1. Introduction

Many kinds of metallic materials have been used in offshore engineering, e.g., shipbuilding and offshore oil platform construction [1,2]. However, it is increasingly difficult to use only conventional metallic materials, e.g., stainless steels, to meet all growing engineering requirements [3]. Compositionally complex alloys (CCAs) possess an excellent combination of properties, making them hopeful candidates for future

* Corresponding author.
** Corresponding author.
E-mail addresses: wyhuo@njfu.edu.cn (W. Huo), fangfeng@seu.edu.cn (F. Fang).

https://doi.org/10.1016/j.jmrt.2022.07.175

engineering applications, such as applications that require high hardness [4], high strength [5,6], strong corrosion resistance [7–9], strong radiation resistance [10], good wear resistance [11], and even superb catalytic properties [12,13]. Among CCAs, medium-entropy alloys (MEAs) have attracted attention as an emerging metallic material [14–18]. Recently, MEAs have received great attention from surface engineering researchers owing to their mechanical properties and corrosion resistance [19–21].

Among the preparation methods of MEAs, electrodeposition is a one-step method to prepare nanocrystalline metallic materials, which is an energy- and cost-saving method. Considering the environmentally hazardous consequences of chromium plating electrolytes [22], the electrodeposition of Cr-free MEAs, e.g., CoNiFe, shows attractive prospects for both environmental friendliness and high performance. In fact, there is a great challenge for the development of electrodeposited MEAs. The major reason for the poor success in the field of electrodeposited MEAs is the complexity of electrolytes required to codeposit multiple elements [19]. There is still limited information about electrodeposited MEAs. In several works on electrodeposited high-entropy alloys (HEAs), there are urgent problems, including a) replacing certain expensive organic ionic liquids or solvents [23–26] and b) obtaining controllable chemical compositions and microstructures [27,28]. On the other hand, the existing results of electrodeposited films of Co-Fe [29], Co-Ni [30], Ni-Fe [31] alloys, and even the results of other binary alloys [32–34] are still valuable for the development of electrodeposited CoNiFe MEAs. For example, it has been widely reported that the current intensity remarkably affects the microstructure and properties of electrodeposited films [35–39]. This provides a simple path for obtaining films with different microstructures. Unfortunately, there is still a lack of information on the corrosion resistance of electrodeposited MEA films, since only a limited amount of work on electrodeposited MEAs has been carried out.

Here, we report the synthesis of a series of highly <111>-oriented CoNiFe MEA films by an electrodeposition process. The resulting films exhibit controllable microstructures and high corrosion resistance and are suitable for applications in offshore engineering.

2. Experimental

2.1. Electrodeposition

First, pure copper was cut into small pieces used for substrates. A series of CoNiFe MEA films were prepared on the substrates at room temperature using direct current electrodeposition. Prior to use, the substrates were polished with grit paper and then cleaned with dilute sulfuric acid. The electrolytic bath consisted of 14.2 mM $CoSO_4$, 76.1 mM $NiSO_4$, 7.2 mM $FeSO_4$, 466.4 mM $C_6H_8O_7$, 163.2 mM $C_6H_5Na_3O_7$, 1.3689 M NaCl, 404.3 mM H_3BO_3, 7.3 mM $C_7H_4NNaO_3S$ and 0.3 mM $C_{12}H_{25}SO_4Na$ (pH 2.5). The electrolytic bath was prepared using ultrapure water. The MEAs were deposited with a varying current density, i.e., 44.4 A/dm^2, 66.7 A/dm^2, 88.9 A/dm^2 and 111.1 A/dm^2. During deposition, a graphite plate was used as the negative electrode, and the solution was degassed with air. The deposition rate was evaluated using weight gain (see Fig. S1).

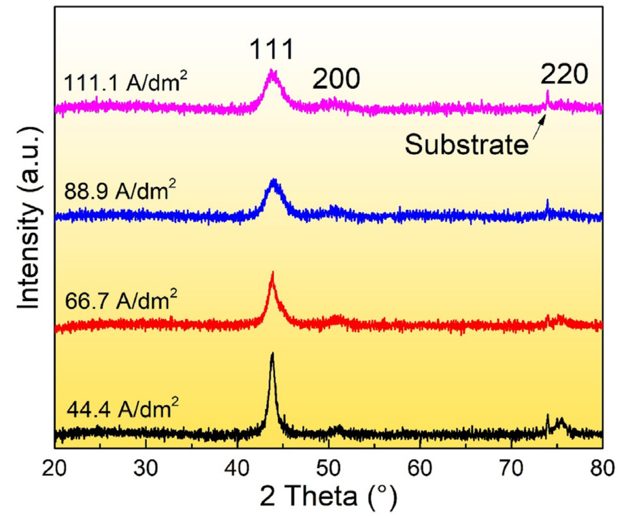

Fig. 1 – XRD patterns of CoNiFe MEA films as a function of current density.

2.2. Structural characterization

The crystal structure of the MEA films was determined by X-ray diffraction (XRD, Rigaku Ultima IV) with Cu $K\alpha$ radiation. The operating voltage was 40 kV, while the operating current was 30 mA. The surface morphology was analyzed using field emission scanning electron microscopy (FE-SEM, Zeiss Merlin Compact and FEI Sirion) equipped with energy dispersive spectrometry (EDS, Oxford Instruments X-Max). The free-standing TEM specimen was mechanically peeled off from the substrate. The microstructure features were also examined in detail by scanning transmission electron microscopy (STEM, Talos F200X) with energy dispersive spectrometry (EDS, Oxford Instruments X-Max) operating at an accelerated voltage of 200 kV.

2.3. Electrocatalytic measurements

Electrochemical tests were carried out using an electrochemical workstation (CHI-760 E) in a 3.5 wt.% NaCl solution at room temperature. Various electrodeposited MEA films were used as working electrodes with an exposed area of 1.0 cm^2. A KCl saturated silver/silver chloride (Ag/AgCl) electrode was selected as the reference electrode, while a platinum mesh was used as the counter electrode. The open circuit potential (OCP) of each sample was continuously monitored for 30 min to obtain a steady potential, and the results were shown in Fig. S2. Electrochemical impedance spectroscopy (EIS) was recorded at 0 V. The frequency range was from 0.1 Hz to 10 MHz, while the sinusoidal perturbation was 5 mV. The EIS data was fitted using a software. Potentiodynamic polarization was carried out with a scanning rate of 1.0 mV/s. The potential was swept from −0.5 V to 0.1 V. The polarization curves were analyzed to acquire the electrochemical parameters using the Tafel extrapolation method.

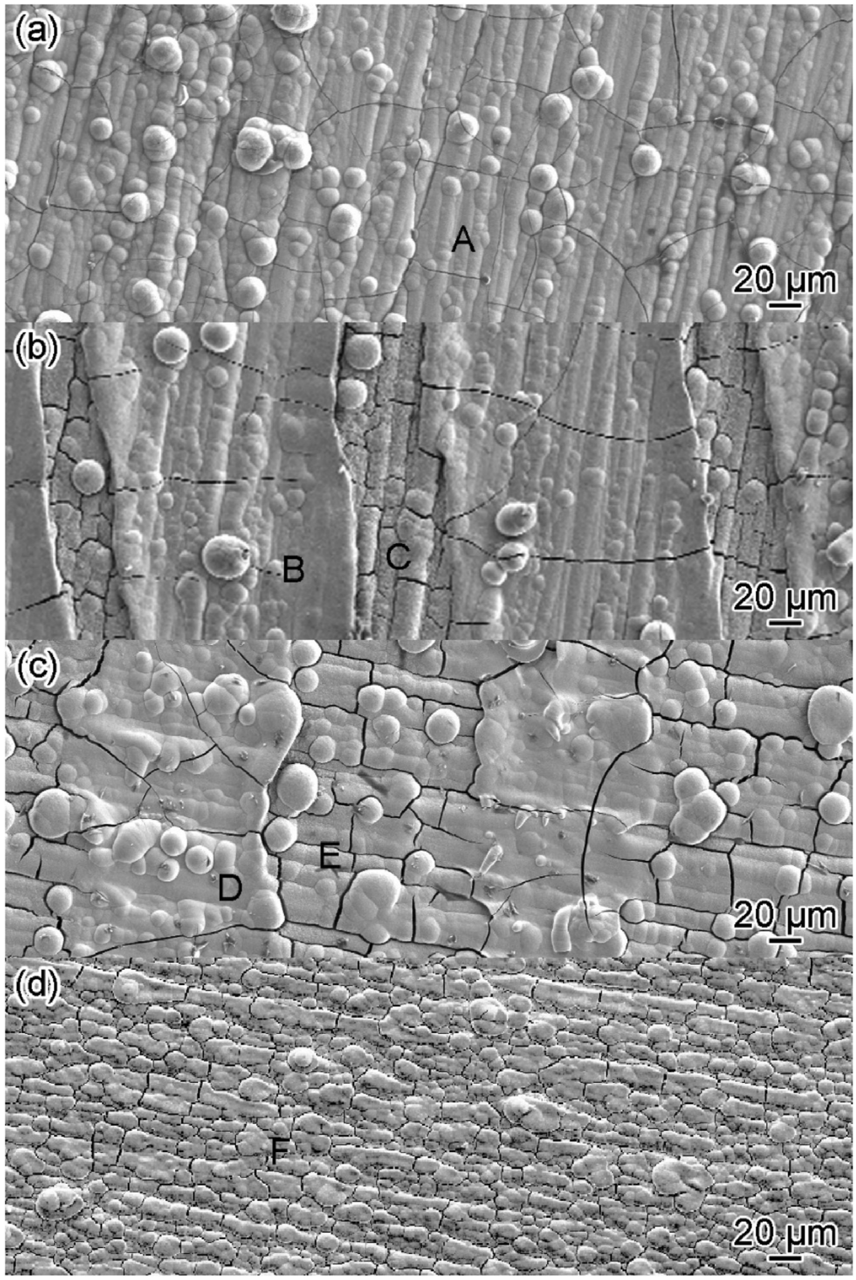

Fig. 2 – SEM images of CoNiFe MEA films with different current densities of (a) 44.4 A/dm^2, (b) 66.7 A/dm^2, (c) 88.9 A/dm^2 and (d) 111.1 A/dm^2.

3. Results

As shown from the XRD patterns in Fig. 1, all MEA films exhibit face-centered cubic (FCC) structures. It shows a strong (111) peak and weak (200) (220) peaks. Furthermore, it was observed that the (111) peaks broadened with an elevated deposition rate. Among all the MEA films, there is a highly <111> preferred orientation. This can be attributed to the reasonable process parameters of direct current electrodeposition.

Fig. 2 shows the surface morphology of the MEA films obtained at different current densities, i.e., 44.4 A/dm^2, 66.7 A/dm^2, 88.9 A/dm^2 and 111.1 A/dm^2. Interestingly, different surface morphologies were developed, depending on the current density. The differences in chemical composition of the microstructure were evaluated with the aid of EDS results, as shown in Table 1. Combined with the XRD results, the MEA film obtained at a low current density of 44.4 A/dm^2 shows near-equimolar ternary components with an FCC structure. The MEA films obtained at a higher current density of 66.7 A/dm^2 and 88.9 A/dm^2 show two FCC phases with different chemical compositions. Ni-rich phase was formed at high current density. When the current density is as high as 111.1 A/dm^2, the MEA film consists entirely of Ni-rich phase. On the other hand, the different crack laws of the two phases can also enable the two phases to be identified. Fig. 3 shows the EDS mapping results of the CoNiFe MEA film with a current density

Table 1 – EDS results of CoNiFe MEA films (at. %).

	Co	Ni	Fe
A	34.5%	33.1%	32.4%
B	38.9%	27.6%	33.5%
C	26.1%	52.3%	21.6%
D	36.5%	25.7%	37.9%
E	20.1%	59.8%	20.1%
F	18.5%	60.9%	20.6%

of 88.9 A/dm^2. It shows the differences between the distribution of elements in the two phases.

Fig. 4 shows the HAADF image and EDS results of the MEA film obtained at a current density of 44.4 A/dm^2. The Co, Ni and Fe element mapping images reveal a uniform chemical composition. In Fig. 5, it shows the HRTEM image. Notably, each bump-like microstructure in the SEM images (Fig. 2) includes a large amount of nanosized grains, which is consistent with the existing works on conventional binary alloys [40–43]. The d-spacing of the grain marked by the yellow line is measured to be 0.206 nm. It is indexed as the plane $(111)_{FCC}$. The typical size of the grain is ~4 nm, which is referenced to the grain marked in yellow.

Polarization curves were measured to study the corrosion behavior of the CoNiFe MEA films in 3.5% NaCl solution (Fig. 6). The self-corrosion current density (i_0) and self-corrosion potential (E_0) were collected from the polarization curves and are listed in Table 2. Notably, although the self-corrosion potentials showed similar values, the self-corrosion current densities became larger with increasing current density. Among all the MEA films, the film with a current density of 44.4 A/dm^2 showed the strongest corrosion resistance in 3.5 wt.% NaCl solution, and its self-corrosion current density was 4.72×10^{-6} A·cm^{-2}. This shows the advantage of the microstructure with a near-equimolar chemical composition.

Fig. 7 shows the EIS test results of MEA films and corresponding fitting curves. In all curves, there was an oblique line in the low-frequency region and a capacity loop in the high-frequency region observed, which can be attributed to the Nernst diffusion-controlled process and the charge transfer process of the corrosion, respectively. R_s [Q (R_{ct}W)] [44] was selected as the equivalent circuit, where R_s was the solution resistance from the reference electrode to the working electrode, Q was the constant phase element, R_{ct} was the charge transfer (Faraday) process, and W was the Warburg impedance controlled by Nernst diffusion.

The calculated values of the elements are listed in Table 3. With the increased current density from 44.4 A/dm^2 to 111.1 A/dm^2, the R_s of the solution resistance almost remained, while Q was increased. Such Q reflected the increase in the double layer capacity [45]. However, the decrease in R_{ct} and W values reflects the acceleration of the charge transfer and Nernst diffusion processes during corrosion. This means that the mechanism turned to the Nernst diffusion controlling process from the mixed-controlling process. The largest value of R_{ct} was 331.2 Ω in the MEA film with a current density of 44.4 A/dm^2. This indicates the large resistivity of the corrosion process in the 3.5 wt.% NaCl solution.

4. Discussion

4.1. *Growth mechanism of electrodeposited MEAs*

The above micrographs of electrodeposited MEAs show different morphologies as a result of simply changing the

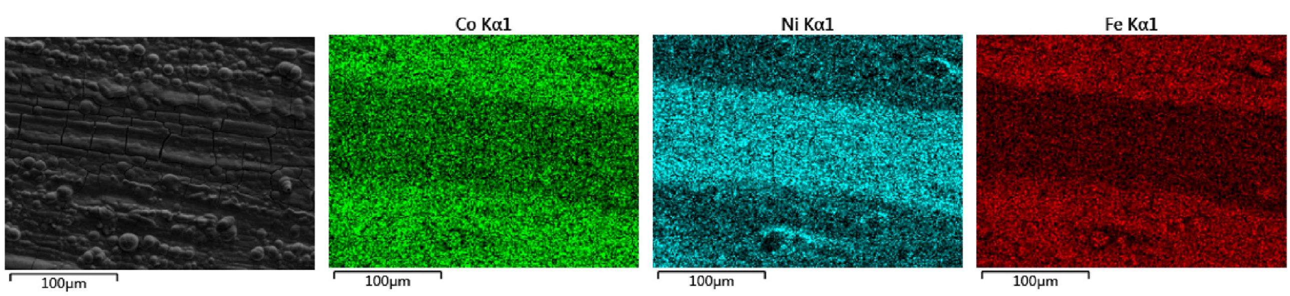

Fig. 3 – EDS mapping results of the CoNiFe MEA film with a current density of 88.9 A/dm^2.

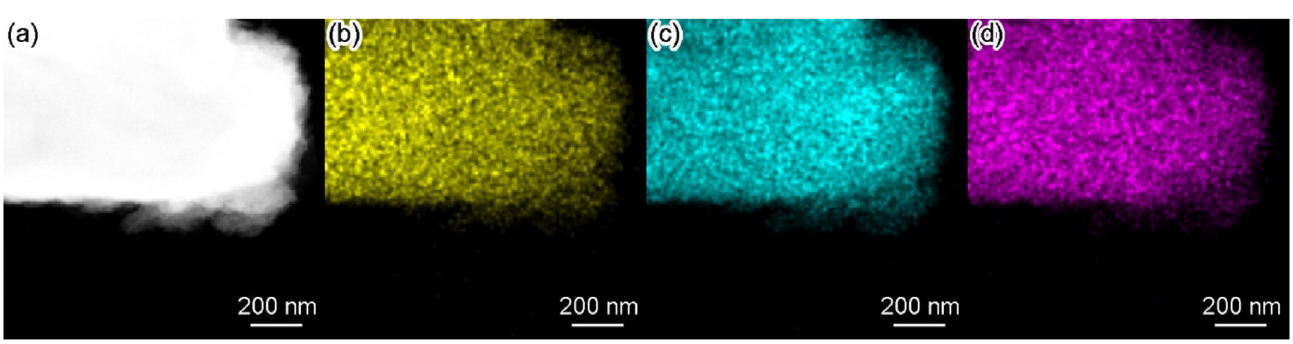

Fig. 4 – HAADF image and EDS mapping results of the MEA film with a current density of 44.4 A/dm^2. (a) HAADF image, (b) Co mapping, (c) Ni mapping and (d) Fe mapping.

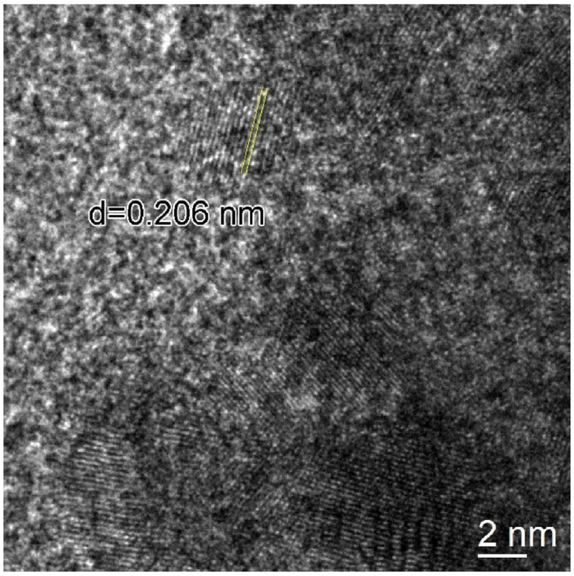

Fig. 5 – HRTEM image of the MEA film with a current density of 44.4 A/dm².

current density. Notably, the nucleation rate depends on the current density during electrodeposition [46]. Thus, the growth cannot be speeded continuously since a higher current density favors nucleation more than growth. At high current densities, there is an excess supply of Ni ions, which leads to nonuniform growth of nucleation perpendicular to the substrate [47]. Crystallization involves the incorporation of adions in the crystal lattice either by the formation of crystals or the building of as-grown crystals [48]. Crystal formation can be promoted by a high adatom population, high overpotential and low surface diffusion rate [49]. With a higher current density, both the adatom population and overpotential increased. As a result, the nucleation rate was increased at high current densities. The rate of nucleation formation, υ, can be described as [50],

Table 2 – Self-corrosion current density (i_0) and self-corrosion potential (E_0) of MEA films with different electrodeposition current densities in 3.5% NaCl solution.

Current density (A/dm²)	i_0 (A·cm⁻²)	E_0 (V v.s)
44.4	4.72×10^{-6}	−0.350
66.7	8.59×10^{-6}	−0.323
88.9	8.72×10^{-6}	−0.306
111.1	1.54×10^{-5}	−0.375

$$\upsilon = K_1 \exp\left(-K_2/_{|\eta|}\right) \quad (1)$$

where K_1 is the proportionality constant, K_2 including the current density is the amount of energy needed for nucleation, and η is the crystallization overpotential. It was inferred that the overpotential increased with the higher current density, and then the nucleation rate was increased. Notably, several works on conventional binary electrodeposited alloys [48,51,52] reported that the chemical composition changes with the current density as different positive ions were present in different concentrations in the bath during electrodeposition. In the current work, there were Co, Ni and Fe ions in different concentrations in the bath. There was phase separation induced by high current densities in the microstructure of electrodeposited MEA films. In fact, it shows a simple method to prepare medium/high entropy composites *in situ*, which is likely to be used to prepare medium/high entropy heterostructures in one step for energy and catalysis applications.

4.2. *Relationship between the microstructure and corrosion resistance in MEAs*

The CoNiFe MEA films deposited at different current densities show various microstructures. The one with a current density of 44.4 A/dm² shows a single FCC phase with a near-equimolar chemical composition. Those with current densities of 66.7 A/dm² and 88.9 A/dm² were medium-entropy composites that consisted of a Ni-rich FCC phase and a Ni-

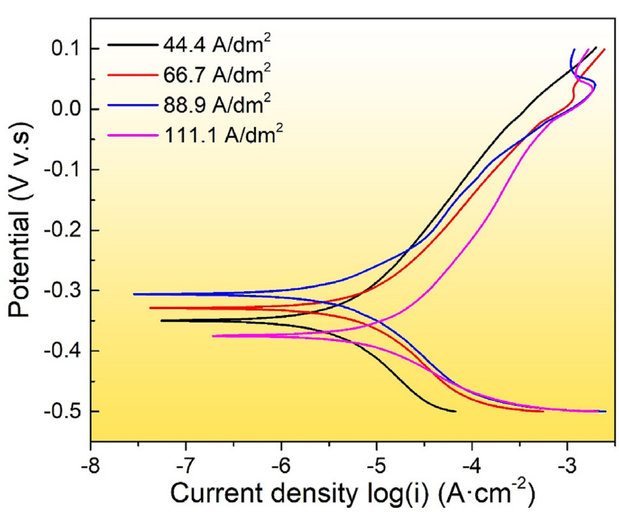

Fig. 6 – Polarization curves of CoNiFe MEA films with different current densities.

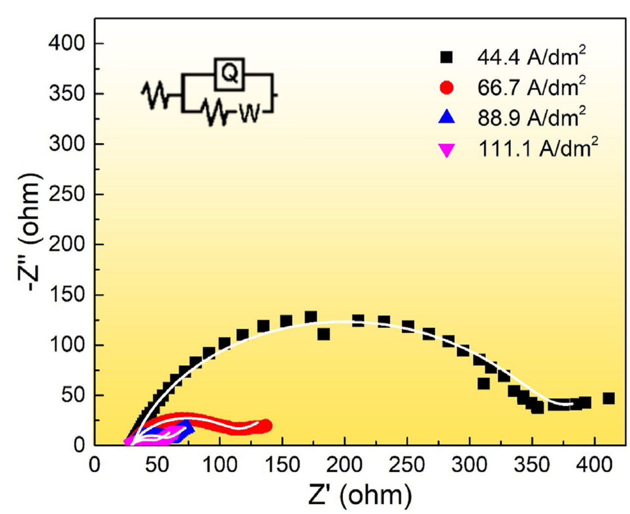

Fig. 7 – EIS test results of CoNiFe MEA films and corresponding fitting curves.

Table 3 – Calculated parameters of the equivalent circuits of the EIS results.

Current density (A/dm^2)	R_s (Ω)	Q ($S\cdot s^n$)	n	R_{ct} (Ω)	W ($S\cdot s^{0.5}$)
44.4	30.05	1.728×10^{-4}	0.8058	331.2	0.03165
66.7	29.43	5.932×10^{-4}	0.7087	84.36	0.04475
88.9	30.05	1.017×10^{-3}	0.7642	26.81	0.05249
111.1	29.57	2.406×10^{-3}	0.6321	19.65	0.07359

poor FCC phase. Another one with a current density of 111.1 A/dm^2 shows a Ni-rich FCC phase. Phase engineering [53] was proposed to obtain excellent performance combinations via different phase structures in CCAs [54,55]. Based on the results in the current work, MEAs with a near-equimolar chemical composition show advantages for anti-corrosion applications. In particular, a 3.5 wt.% NaCl solution was selected as the corrosive medium. A 3.5 wt.% NaCl solution is widely considered for use in anti-corrosion materials for marine applications, as its pH and chloride level are very comparable to those of sea water.

Notably, the electrodeposited nanocrystalline CoNiFe MEA with a highly <111> orientation shows a low self-corrosion current density and a self-corrosion potential, e.g., 4.72×10^{-6} $A\cdot cm^{-2}$ and −0.350 V in the MEA with a current density of 44.4 A/dm^2. Electrodeposited CoNiFe MEAs show greater anti-corrosion properties than 700 °C × 1 h-annealed, cold-rolled CoNiFe MEAs with a self-corrosion current density of 2.34×10^{-5} $A\cdot cm^{-2}$ [8]. The outstanding anti-corrosion properties distinguish the electrodeposited MEA films from currently available MEAs, meaning that if MEAs are prepared using a specific electrodeposition process, the MEAs can have potential for anti-corrosion applications.

5. Conclusions

In summary, we united the microstructure and corrosion resistance of CoNiFe MEA films with varying deposition current densities. The films show the FCC structure with a <111> preferential orientation. It shows a low self-corrosion current density of 4.72×10^{-6} $A\cdot cm^{-2}$ in a 3.5 wt.% NaCl solution. The corrosion mechanism was proposed in combination with EIS results. The outstanding properties were attributed to the near-equimolar ternary components. The results lay a solid foundation for the development of highly oriented MEA films with strong corrosion resistance.

CRediT authorship contribution statement

W.Y. Huo: Conceptualization, Methodology, Investigation, Writing - original draft, Writing - review & editing, Supervision. S.Q. Wang: Investigation, Formal analysis. F. Fang: Writing - review & editing, Supervision. S.Y. Tan: Formal analysis. Ł. Kurpaska: Writing - review & editing. Z. Xie: Writing - review & editing. H.S. Kim: Writing - review & editing. J.Q. Jiang: Writing - review & editing.

Declaration of Competing Interest

The authors declare that they have no known competing financial interests or personal relationships that could have appeared to influence the work reported in this paper.

Acknowledgements

The work was supported by Jiangsu Province Natural Science Foundation, China (BK20220428), National Natural Science Foundation of China, China (52171110), Natural Science Foundation of the Jiangsu Higher Education Institutions of China, China (21KJB430014), Jiangsu Key Laboratory of Advanced Structural Materials and Application Technology Project, China (ASMA202104), and Metasequoia Faculty Research Funding of Nanjing Forestry University, China (163040160). W.Y. Huo acknowledges the support from Advanced Analysis and Testing Center, Nanjing Forestry University, China. Z. Xie acknowledges the support provided by the Australian Research Council Discovery Projects, Australia.

Appendix A. Supplementary data

Supplementary data to this article can be found online at https://doi.org/10.1016/j.jmrt.2022.07.175.

REFERENCES

[1] Zhang TY, Liu W, Chen LJ, Dong BJ, Yang WJ, Fan YM, et al. On how the corrosion behavior and the functions of Cu, Ni and Mo of the weathering steel in environments with different NaCl concentrations. Corrosion Sci 2021;192:109851.

[2] Su BX, Wang BB, Luo LS, Wang L, Su YQ, Xu YJ, et al. Effect of zirconium content on the microstructure and corrosion behavior of as-cast Ti-Al-Nb-Zr-Mo alloy. J Mater Res Technol 2021;15:4896–913.

[3] Zhu M, He F, Yuan YF, Guo SY, Wei GY. A comparative study on the corrosion behavior of CoCrNi medium-entropy alloy and 316L stainless steel in simulated marine environment. Intermetallics 2021;139:107370.

[4] Huo WY, Fang F, Liu XD, Tan SY, Xie ZH, Jiang JQ. Remarkable strain-rate sensitivity of nanotwinned CoCrFeNi alloys. Appl Phys Lett 2019;114:101904.

[5] Ding QQ, Fu XQ, Chen DK, Bei HB, Gludovatz B, Li JX, et al. Real-time nanoscale observation of deformation mechanisms in CrCoNi-based medium- to high-entropy alloys at cryogenic temperatures. Mater Today 2019;25:21–7.

[6] Huo WY, Fang F, Zhou H, Xie ZH, Shang JK, Jiang JQ. Remarkable strength of CoCrFeNi high-entropy alloy wires at cryogenic and elevated temperatures. Scripta Mater 2017;141:125–8.

[7] Kao Y-F, Lee T-D, Chen S-K, Chang Y-S. Electrochemical passive properties of $Al_xCoCrFeNi$ (x = 0, 0.25, 0.50, 1.00) alloys in sulfuric acids. Corrosion Sci 2010;52:1026–34.

[8] An XL, Chen CL, Zhou L, Ji J, Shen BL, Chu PK. Controlling the corrosion behavior of CoNiFe medium entropy alloy by grain boundary engineering. Mater Char 2020;164:110323.

[9] Kumar N, Fusco M, Komarasamy M, Mishra RS, Bourham M, Murty KL. Understanding effect of 3.5 wt.% NaCl on the corrosion of $Al_{0.1}$CoCrFeNi high-entropy alloy. J Nucl Mater 2017;495:154–63.
[10] El-Atwani O, Li N, Li M, Devaraj A, Baldwin JKS, Schneider MM, et al. Outstanding radiation resistance of tungsten-based high-entropy alloys. Sci Adv 2019;5:eaav2002.
[11] Chen M, Shi XH, Yang HJ, Liaw PK, Gao MC, Hawk JA, et al. Wear behavior of $Al_{0.6}$CoCrFeNi high-entropy alloys: effect of environments. J Mater Res 2018;33:3310–20.
[12] Wang SQ, Huo WY, Fang F, Xie ZH, Shang JK, Jiang JQ. High entropy alloy/C nanoparticles derived from polymetallic MOF as promising electrocatalysts for alkaline oxygen evolution reaction. Chem Eng J 2022;429:132410.
[13] Wang SQ, Xu BL, Huo WY, Feng HC, Zhou XF, Fang F, et al. Efficient FeCoNiCuPd thin-film electrocatalyst for alkaline oxygen and hydrogen evolution reactions. Appl Catal B Environ 2022;313:121472.
[14] Yang Y, Chen TY, Tan LZ, Poplawsky JD, An K, Wang YL, et al. Bifunctional nanoprecipitates strengthen and ductilize a medium-entropy alloy. Nature 2021;595:245–9.
[15] Gludovatz B, Hohenwarter A, Thurston KVS, Bei HB, Wu ZG, George EP, et al. Exceptional damage-tolerance of a medium-entropy alloy CrCoNi at cryogenic temperatures. Nat Commun 2016;7:10602.
[16] Zhao YL, Yang T, Tong Y, Wang J, Luan JH, Jiao ZB, et al. Heterogeneous precipitation behavior and stacking-fault-mediated deformation in a CoCrNi-based medium-entropy alloy. Acta Mater 2017;138:72–82.
[17] Yan XH, Zhang Y. A body-centered cubic $Zr_{50}Ti_{35}Nb_{15}$ medium-entropy alloy with unique properties. Scripta Mater 2020;178:329–33.
[18] Ma Y, Yuan FP, Yang MX, Jiang P, Ma E, Wu XL. Dynamic shear deformation of a CrCoNi medium-entropy alloy with heterogeneous grain structures. Acta Mater 2018;148:407–18.
[19] Haché MJR, Tam J, Erb U, Zou Y. Electrodeposited nanocrystalline medium-entropy alloys – an effective strategy of producing stronger and more stable nanomaterials. J Alloys Compd 2022;899:163233.
[20] Feng K, Zhang Y, Li ZG, Yao CW, Yao L, Fan CY. Corrosion properties of laser cladded CrCoNi medium entropy alloy coating. Surf Coat Technol 2020;397:126004.
[21] Hu M, Cao QP, Wang XD, Zhang DX, Jiang J-Z. Ultra-strong nanostructured Co-Ni-V medium entropy alloy thin film designed by interface strengthening. Thin Solid Films 2021;734:138866.
[22] Huo WY, Wang SQ, Zhang XH, Ren K, Tan SY, Fang F, et al. A strategy to improve the performance of TiO_2 nanotube array film photocatalysts by magnetron-sputtered amorphous $BiFeO_3$. Vacuum 2022;202:111135.
[23] Huang J, Du K, Wang P, Yin H, Wang D. Electrochemical preparation and homogenization of face-centered FeCoNiCu medium entropy alloy electrodes enabling oxygen evolution reactions. Electrochim Acta 2021;378:138142.
[24] Yoosefan F, Ashrafi A, Monir vaghefi SM, Constantin I. Synthesis of CoCrFeMnNi high entropy alloy thin films by pulse electrodeposition: Part 1: effect of pulse electrodeposition parameters. Met Mater Int 2020;26:1262–9.
[25] Soare V, Burada M, Constantin I, Mitrică D, Bădiliţă V, Caragea A, et al. Electrochemical deposition and microstructural characterization of AlCrFeMnNi and AlCrCuFeMnNi high entropy alloy thin films. Appl Surf Sci 2015;358:533–9.
[26] Yao C-Z, Zhang P, Liu M, Li G-R, Ye J-Q, Liu P, et al. Electrochemical preparation and magnetic study of Bi–Fe–Co–Ni–Mn high entropy alloy. Electrochim Acta 2008;53:8359–65.
[27] Aliyu A, Srivastava C. Microstructure and electrochemical properties of FeNiCoCu medium entropy alloy-graphene oxide composite coatings. J Alloys Compd 2021;864:158851.
[28] Aliyu A, Srivastava C. Microstructure-corrosion property correlation in electrodeposited AlCrFeCoNiCu high entropy alloys-graphene oxide composite coatings. Thin Solid Films 2019;686:137434.
[29] Kockar H, Alper M, Sahin T, Karaagac O. Role of electrolyte pH on structural and magnetic properties of Co–Fe films. J Magn Magn Mater 2010;322:1095–7.
[30] Badawy WA, Nady H, Negem M. Cathodic hydrogen evolution in acidic solutions using electrodeposited nano-crystalline Ni–Co cathodes. Int J Hydrogen Energy 2014;39:10824–32.
[31] Cheung C, Djuanda F, Erb U, Palumbo G. Electrodeposition of nanocrystalline Ni-Fe alloys. Nanostruct Mater 1995;5:513–23.
[32] Aghdam AS, Allahkaram SR, Mahdavi S. Corrosion and tribological behavior of Ni–Cr alloy coatings electrodeposited on low carbon steel in Cr (III)–Ni (II) bath. Surf Coat Technol 2015;281:144–9.
[33] Saravanan G, Mohan S. Structure, composition and corrosion resistance studies of Co–Cr alloy electrodeposited from deep eutectic solvent (DES). J Alloys Compd 2012;522:162–6.
[34] Tang LP, Wu W, He LB, Xu T, Dong H, Zhang L, et al. In situ observation of the solid solution-induced sublimation of CuAg Janus nanoparticles. J Alloys Compd 2021;877:160168.
[35] Wang F, Watanabe T. Preparation and characterization of the electrodeposited Fe–Cr alloy film. Mater Sci Eng, A 2003;349:183–90.
[36] Qiao GY, Jing TF, Wang N, Gao YW, Zhao X, Zhou JF, et al. High-speed jet electrodeposition and microstructure of nanocrystalline Ni–Co alloys. Electrochim Acta 2005;51:85–92.
[37] Lew KS, Raja M, Thanikaikarasan S, Kim T, Kim YD, Mahalingam T. Effect of pH and current density in electrodeposited Co–Ni–P alloy thin films. Mater Chem Phys 2008;112:249–53.
[38] Özdemir R, Karahan İH, Karabulut O. A study on the electrodeposited Cu-Zn alloy thin films. Metall Mater Trans A 2016;47:5609–17.
[39] Wasekar NP, Haridoss P, Seshadri SK, Sundararajan G. Influence of mode of electrodeposition, current density and saccharin on the microstructure and hardness of electrodeposited nanocrystalline nickel coatings. Surf Coat Technol 2016;291:130–40.
[40] Sheikholeslam MA, Enayati MH, Raeissi K. Characterization of nanocrystalline and amorphous cobalt–phosphorous electrodeposits. Mater Lett 2008;62:3629–31.
[41] Ghaferi Z, Raeissi K, Golozar MA, Edris H. Characterization of nanocrystalline Co–W coatings on Cu substrate, electrodeposited from a citrate-ammonia bath. Surf Coat Technol 2011;206:497–505.
[42] Sakita AMP, Passamani EC, Kumar H, Cornejo DR, Fugivara CS, Noce RD, et al. Influence of current density on crystalline structure and magnetic properties of electrodeposited Co-rich CoNiW alloys. Mater Chem Phys 2013;141:576–81.
[43] Liu JH, Li WH, Pei ZL, Gong J, Sun C. Investigations on the structure and properties of nanocrystalline Ni-Mo alloy coatings. Mater Char 2020;167:110532.
[44] Bo X, Tang AY, Dou ML, Li ZL, Wang F. Controllable electrodeposition and mechanism research of nanostructured Bi_2Te_3 thin films with high thermoelectric properties. Appl Surf Sci 2019;486:65–71.
[45] Hitz C, Lasia A. Experimental study and modeling of impedance of the HER on porous Ni electrodes. J Electroanal Chem 2001;500:213–22.

[46] Deo Y, Guha S, Sarkar K, Mohanta P, Pradhan D, Mondal A. Electrodeposited Ni-Cu alloy coatings on mild steel for enhanced corrosion properties. Appl Surf Sci 2020;515:146078.
[47] Augustin A, Udupa KR, Bhat KU. Effect of coating current density on the wettability of electrodeposited copper thin film on aluminum substrate. Perspect Sci 2016;8:472–4.
[48] Allahyarzadeh MH, Ashrafi A, Golgoon A, Roozbehani B. Effect of pulse plating parameters on the structure and properties of electrodeposited Ni-Mo films. Mater Chem Phys 2016;175:215–22.
[49] Choo RTC, Toguri JM, El-Sherik AM, Erb U. Mass transfer and electrocrystallization analyses of nanocrystalline nickel production by pulse plating, Mass transfer and electrocrystallization analyses of nanocrystalline nickel production by pulse plating. J Appl Electrochem 1995;25:384–403.
[50] Chandrasekar MS, Pushpavanam M. Pulse and pulse reverse plating—conceptual, advantages and applications. Electrochim Acta 2008;53:3313–22.
[51] Agarwal M, Kumar V, Malladi S, Balasubramaniam R, Balani K. Effect of current density on the pulsed co-electrodeposition of nanocrystalline nickel-copper alloys. JOM 2010;62:88–92.
[52] Mousavi R, Raeissi K, Saatchi A. The effect of pH on the properties of Ni-Mo nanocrystalline electrodeposits. Int J Mod Phys B 2008;22:3060–8.
[53] Chang XJ, Zeng MQ, Liu KL, Fu L. Phase engineering of high-entropy alloys. Adv Mater 2020;32:1907226.
[54] Huo WY, Wang SQ, Zhu WH, Zhang ZL, Fang F, Xie ZH, et al. Recent progress on high-entropy materials for electrocatalytic water splitting applications. Tungsten 2021;3:161–80.
[55] Zhu WH, Huo WY, Wang SQ, Wang X, Ren K, Tan SY, et al. Phase formation prediction of high-entropy alloys: a deep learning study. J Mater Res Technol 2022;18:800–9.